Urban Seismic Site Characterization by Fiber-Optic Seismology

Zack J. Spica[1,2] [ID], Mathieu Perton[3] [ID], Eileen R. Martin[4] [ID], Gregory C. Beroza[5] [ID], and Biondo Biondi[5] [ID]

[1]Department of Earth and Environmental Sciences, University of Michigan, Ann Arbor, MI, USA, [2]Formerly at Department of Geophysics, Stanford University, Stanford, CA, USA, [3]Instituto de Ingeniería, Universidad Nacional Autónoma de México, CDMX, Mexico, [4]Department of Mathematics, Program in Computational Modeling and Data Analytics, Virginia Tech, Blacksburg, VA, USA, [5]Department of Geophysics, Stanford University, Stanford, CA, USA

Abstract Accurate ground motion prediction requires detailed site effect assessment, but in urban areas where such assessments are most important, geotechnical surveys are difficult to perform, limiting their availability. Distributed acoustic sensing (DAS) offers an appealing alternative by repurposing existing fiber-optic cables, normally employed for telecommunication, as an array of seismic sensors. We present a proof-of-concept demonstration by using DAS to produce high-resolution maps of the shallow subsurface with the Stanford DAS array, California. We describe new methods and their assumptions to assess H/V spectral ratio—a technique widely used to estimate the natural frequency of the soil—and to extract Rayleigh wave dispersion curves from ambient seismic field. These measurements are jointly inverted to provide models of shallow seismic velocities and sediment thicknesses above bedrock in central campus. The good agreement with an independent survey validates the methodology and demonstrates the power of DAS for microzonation.

1. Introduction

Rapid population growth has increased the concentration of people, buildings, and infrastructure in urban areas. Many of these urban centers are developed atop sedimentary basins in earthquake-prone regions, which increases their vulnerability to earthquakes due to the presence of soft sediments that amplify and extend earthquake shaking. Soil conditions are known to have a significant influence on ground motion and damage in earthquakes, as has been well documented in the 1985 Michoacán, Mexico, and 1995 Kobe, Japan earthquakes, among many others. As a result, seismic building codes (Federal Emergency Management Agency, 2003) include a soil classification to capture the effects of shallow site response (i.e., resonance frequency) and shear-wave velocity (i.e., $V_S 30$) on ground motion.

One of the most widely used techniques to estimate seismic site response involves analyzing the horizontal-to-vertical spectral ratio (HVSR) (Nakamura, 1989) of ambient seismic field recordings. The originally proposed justification for this method is that larger amplitude shear waves would be principally responsible for the ground motion at a site, and most of their energy is recorded as horizontal motion. Thus, peaks in the spectral ratio represent frequencies that experience local shear-wave amplification. The diffuse wavefield approach (Sánchez-Sesma et al., 2011) provides a theoretical framework for modeling H/V spectral ratio observations and a means to use them to estimate reliable shallow V_S models (e.g., Lontsi et al., 2015; Perton et al., 2017, Rivet et al., 2015; Salinas et al., 2014; Spica et al., 2015, 2017; Thomas et al., 2019), which are essential for ground motion prediction. Because it is straightforward to perform, HVSR has become a cornerstone of seismic microzonation (e.g., Bard, 1998; Stanko et al., 2017; Tumurbaatar et al., 2019).

Even though a typical H/V measurement requires only a few tens of minutes of ambient seismic field recording using a tri-axial seismometer, the potential resolution of H/V microzonation at the scale of a city is limited by the distribution of available measurements due to two main factors: (1) the money/time available for field campaign and (2) the complex physical, geographical, and legal logistics inherent to urban settings. Both of these limitations have prevented urban microzonation with H/V spectral ratio from reaching its full potential.

In this paper we present an alternative approach that can overcome these limitations through distributed acoustic sensing (DAS) using underground fiber-optic cable repurposed as a seismometer array with
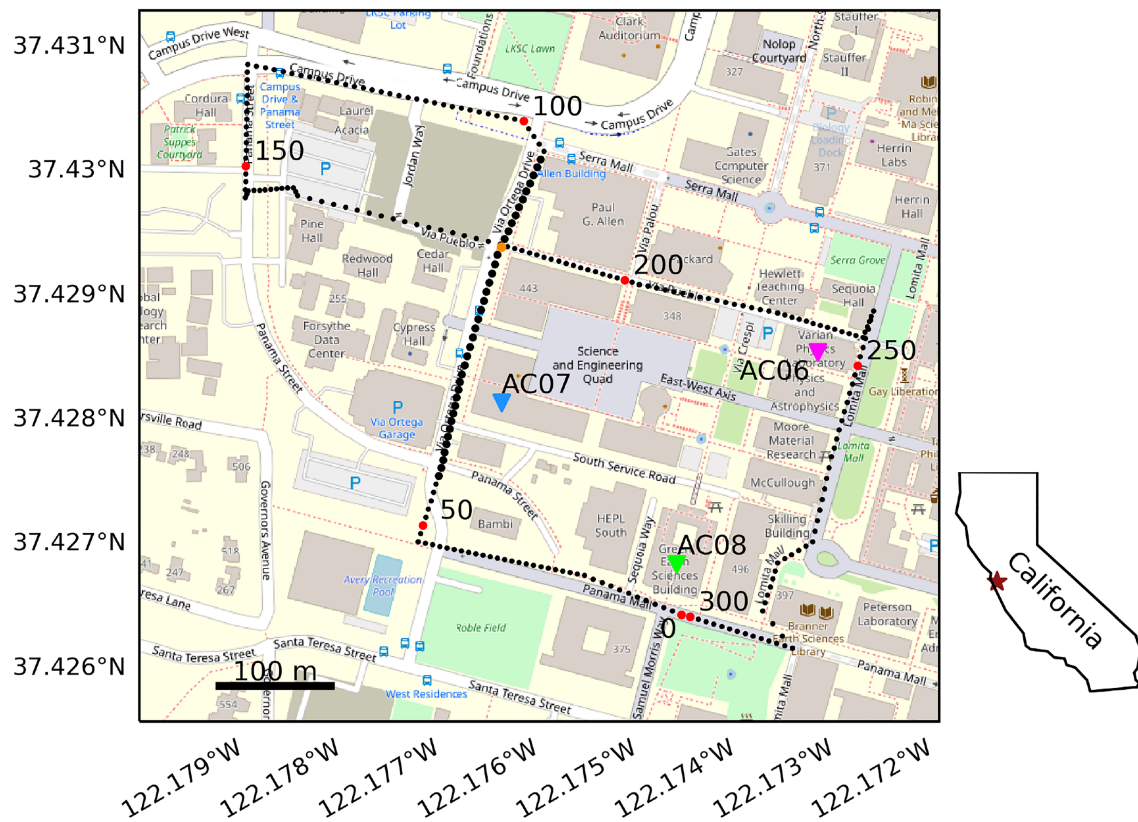
Figure 1. Map of the Stanford DAS array. Map of the Stanford University campus (West central campus, overlaid on map from OpenStreetMap) and the fiber-optic array. Each black dot represents the center of a channel along the fiber where a strain measurement is performed. They are spaced at approximately 8 m intervals and numbered from 0 to 300. The multiples of 50 are highlighted with a red dot. Only the 300 (out of 620) first channels are shown as the cable loops twice around its track for overlapping measurements. In this study, we focus on channels 55 to 95 that are located along the Via Ortega Drive and highlighted by thicker black dots. The orange dot depicts the intersection between Via Ortega Drive and Via Pueblo where channels 85 and 185 are orthogonal but co-located. The three inverted triangles depict the velocimeters (i.e., broadband seismometers after removing their instrumental response) used in this study.

a measurement density on the order of meters. DAS systems rely on coherent optical time-domain reflectometry to measure the amplitude and phase of vibrations along a fiber (Grattan & Sun, 2000). DAS is used in the oil and gas industry for seismic profiling (e.g., Lellouch, Horne, et al., 2019; Mateeva et al., 2012), microseismic monitoring (Webster et al., 2013), and time-lapse seismic surveys (Daley et al., 2013). Its recent applications to passive earthquake seismology have demonstrated the consistency between earthquake waveforms recorded by DAS and by conventional seismometers (e.g., Ajo-Franklin et al., 2019; Biondi et al., 2017; Lindsey et al., 2017; Wang et al., 2018). DAS response has been shown to be broadband, even when using existing telecommunication infrastructure not deployed for seismic monitoring (e.g., Biondi et al., 2017; Jousset et al., 2018; Sladen et al., 2019; Yu et al., 2019). Finally, Yu et al. (2019) showed it was possible to compute receiver functions by deconvolving vertical component velocity seismograms from DAS strain recordings.

We demonstrate that H/V spectral ratio measurements can be performed with DAS and that it provides reliable geotechnical information in an urban environment with a density that would be difficult to obtain through a standard microzonation campaign. In addition, we extract Rayleigh wave phase dispersion curves from these measurements using ambient-field interferometry and jointly invert these two observables to infer simple but reliable velocity models of the shallow subsurface with resolution at depth that should be superior to conventional geotechnical surveys. Our approach can be used to extract almost continuous V_S profiles along a fiber cable network and could eventually be repeated through time at little additional cost. We illustrate our method using the Stanford DAS array (Figure 1), which consists of a fiber cable laying in an air-filled PVC conduit (no clamping or cementing) (Martin et al., 2017). Our results suggest that if a standard velocimeter (i.e, seismometer) is close to a DAS array, similar analysis could be performed on many existing fiber-optic networks around the world.

2. Materials and Methods

2.1. The Stanford DAS Array

DAS uses a standard fiber-optic cable as both an axial strain sensor and a means of transmitting its own data to a storage unit. An interrogator probes the cable via a laser pulse, and an interferometer measures the amount of light back-scattered from the heterogeneities (or scatterers) naturally created during the fiber manufacturing process. Such measurement is performed by counting photons within a gauge length and the resulting phase shift is quasi-linearly proportional to the total axial strain change (caused by either axial dilation or compression) along this section of the fiber (Grattan & Sun, 2000). DAS has a lower signal to noise ratio and a stronger angular sensitivity than standard seismometers; however, this drawback is largely compensated by the benefits of having an ultradense series of permanently installed and highly resistant seismic sensors communicating over large distances and running on a single power source (Martin et al., 2018).

The Stanford DAS array was created using a fiber cable loosely deployed in an air-filled PVC conduit (~12 cm wide) managed by Stanford IT Services (Figure 1). The coupling between the cable and the surrounding rock relies therefore exclusively on gravity and friction. The Stanford DAS array recorded and stored continuous data from 620 independent seismic channels at a frequency of 50 samples per second with 7.14 m gauge length and 8.16 m channel spacing. Through this experiment Martin et al. (2017) showed that DAS technology can be used to record seismic data directly from a free-floating cable in a horizontal PVC conduit. Furthermore, by analyzing adjacent earthquakes on nearby faults, Biondi et al. (2017) demonstrated that signals recorded using this cable provide repeatable and reliable ground motion measurements. More details about the array design, geometry, and setup can be found in Biondi et al. (2017) or in Martin et al. (2017).

Two different interrogator units were installed at Stanford: OptaSense ODH-3 and ODH-4. ODH-3 started recording signals in early September 2016 and was used to compute year-long dispersion curves (section 2.4). ODH-4 only recorded a few days of seismic data between 5 October 2017 and 13 October 2017. These data were acquired along with ODH-3 and three broadband seismometers temporarily installed near the array (USGS, 2016). As ODH-4 recordings show a higher data quality (supporting information, Figure S1), it was used to compute the HVSR with DAS. In what follows, we will refer to the broadband seismometers as velocimeters since, after removal of their instrument response, they record the velocity of ground motion.

2.2. From Strainmeter to Virtual Velocimeter

The strain component measured at a channel is the spatial derivative of the displacement along the cable denoted locally as the direction e_x: $\varepsilon_{xx} = u_{x,x}$. Using a plane wave decomposition $\mathbf{u}(x, t) = \mathbf{U}e^{\iota(\mathbf{kx}-\omega t)}$, we can express the strain component as $\varepsilon_{xx} = \iota k_x u_x$, where $\mathbf{k}$, ω, ι, and $\mathbf{x}$ are the wave number vector, the angular frequency, the imaginary number, and the position, respectively. Since the particle velocity is the time derivative of the displacement ($v_x = \dot{u}_x = \frac{du_x}{dt} = -\iota\omega u_x$), we obtain the relationship linking strain to particle velocity as $\varepsilon_{xx} = \iota k_x u_x = -\frac{k_x}{\omega}\dot{u}_x$; and as the modes propagate along the surface in the direction e_x with a phase velocity given by $c = \frac{\omega}{k_x(\omega)}$, previous studies (e.g., Wang et al., 2018; Yu et al., 2019) used

$$\varepsilon_{xx} = -\frac{1}{c}v_x \tag{1}$$

to compare DAS strain to velocimeter records.

In equation (1), k_x depends on ω according to the different modes and depends on both the subsurface velocity structure and the wavefront's angle of incidence. As the fundamental Rayleigh wave mode always has the highest k_x for any frequency (ignoring Love waves), it is strongly amplified by the DAS measurement. The latter is illustrated by the theoretical $\omega - k_x$ diagrams for both strain and velocity (Figure 2) in which we observe that the first Rayleigh mode dominates the strain spectrum. Figure 2 is obtained using an averaged V_S velocity model for central campus (Figure S3) previously produced by an independent study and based on spectral analysis of surface waves (Thomas et al., 2014). The calculation was performed using the discrete wave number method (Bouchon, 2003). The bright colors in the figure correspond to higher amplitudes.

The phase velocity c modulates the seismogram recorded by DAS and has a major effect on the amplitude. Because c varies generally smoothly, its effect on the phase of the signal is muted, which explains the success of previous travel time-based analyses, using both local and teleseismic earthquakes or ambient seismic field directly with DAS strain recordings (Yu et al., 2019; Zeng et al., 2017). Because body waves have almost
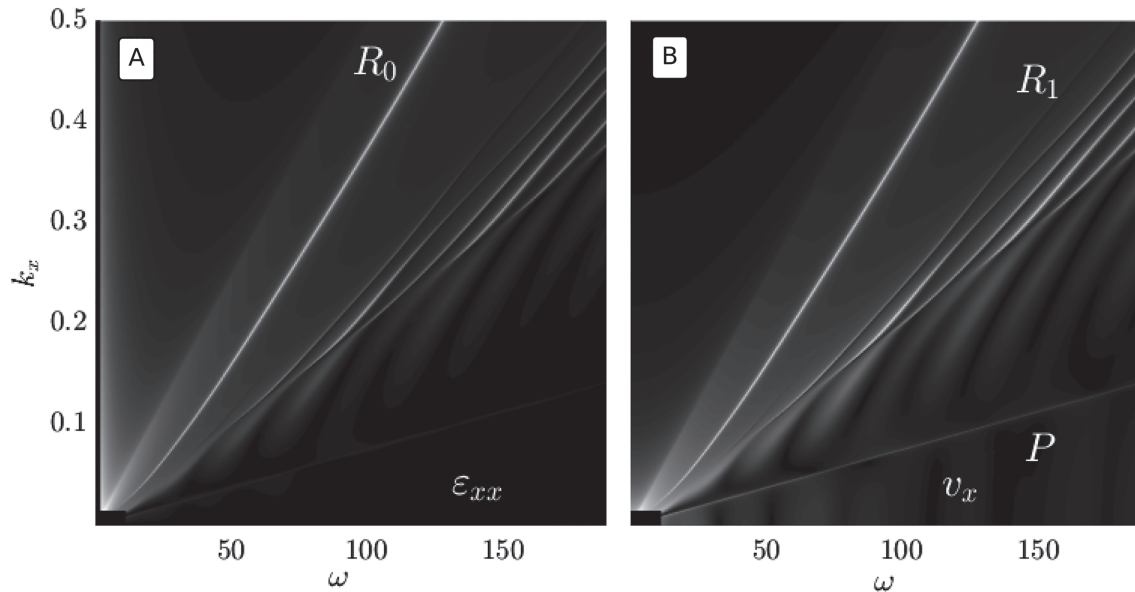
Figure 2. $\omega - k_x$ diagrams for strain and velocity. (a) Strain $\omega - k_x$ diagram. (b) Velocity $\omega - k_x$ diagram. Both diagrams are obtained by simulating the wave propagation with the discrete wave number method using velocity model shown in Figure S3. The gray scale is logarithmic and light colors correspond to higher energies. R_0 and R_1 indicate the fundamental and first higher mode of the Rayleigh wave, respectively. P is the P-wave.

no dispersion, DAS measurements allow measurement of their travel times directly from strain records (e.g., Lellouch et al., 2019a, 2019b; Lellouch, Yuan, et al., 2019).

Equation (1) can be used to retrieve the phase velocity of the fundamental Rayleigh wave (c_{R_0}) if both v_x (from a velocimeter) and ε_{xx} (from DAS) measurements are available at a site (e.g., Yu et al., 2019). The particle velocity of the fundamental Rayleigh mode is calculated by applying the transformation $v_x = -c_{R_0}\varepsilon_{xx}$ to DAS measurements (Wang et al., 2018; Yu et al., 2019); however, by doing so, it is important to keep in mind that we artificially enhance the contribution of the Rayleigh mode compared to amplitudes measured by a traditional velocity sensor. Other factors such as the gauge length, the angle of incidence of the wavefield, and the coupling of the fiber with the ground may also influence the amplitude.

We can compare DAS and velocimeter measurements (Figure 3) by converting strain to particle velocity using a theoretical Rayleigh phase dispersion curve obtained from the velocity model showed in Figure S3. This comparison is conducted for both ambient seismic field and earthquake waveforms in both time and spectral domains with reference to velocimeter AC07. The ambient seismic field is recorded at one of the closest channels to station AC07 (channel 70, which is ~30 m distant) while the earthquake (8 October 2017 01:40:15, Md 2.8, 36.847° N 121.577° W, next to Hollister, CA) is recorded at channel 185 with orientation closer to the wave propagation direction. Channel 185 is ~120 m away from AC07 and is located on Via Ortega Drive but is orthogonal to the direction of the road (parallel to Via Pueblo; orange dot in Figure 1). To facilitate the comparison, waveforms of the horizontal components of the station AC07 were corrected for instrument response and rotated according to the fiber orientation. DAS clearly records the ambient seismic field and earthquake waveforms with comparable phase and amplitude to the seismometer (e.g., Lindsey et al., 2017; Yu et al., 2019). Although the signal to noise ratio of DAS is lower than conventional broadband sensors, transient signals of small amplitude can be recorded with a single channel, as observed around 30 s time lag in Figure 3a.

2.3. The H/V Spectral Ratio with DAS
2.3.1. HVSR for a Diffuse Wavefield
In its simplest form, the H/V spectral ratio is the square root of the ratio of the spectral energy components of a tri-axial ground motion sensor (Arai & Tokimatsu, 2004):

$$\frac{H}{V}(\mathbf{x}, \omega) = \sqrt{\frac{E_1(\mathbf{x}, \omega) + E_2(\mathbf{x}, \omega)}{E_3(\mathbf{x}, \omega)}}, \qquad (2)$$
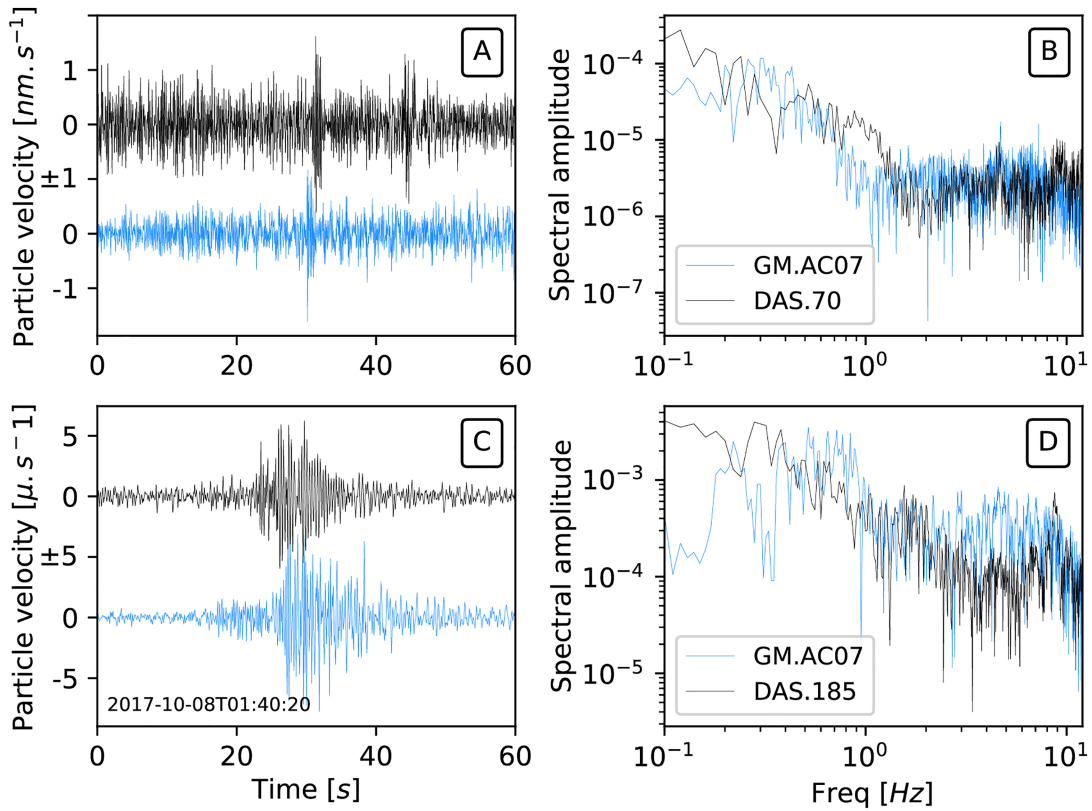
Figure 3. Velocity-converted waveforms. Velocity-converted waveforms from DAS (black) and station AC07 (blue). DAS waveforms are converted from strain to velocity using equation (1), and the geophone waveforms are corrected for instrument response and rotated according to the orientation of the DAS measurement. (a) Sixty seconds of ambient seismic field recording (with DAS channel 70), bandpass filtered between 0.8 and 8 Hz. (b) Amplitude spectra of the unfiltered waveforms shown in (a). (c) M_d 2.8 earthquake (recorded with DAS channel 185), bandpass filtered between 0.8 and 8 Hz. (d) Amplitude spectra of the unfiltered waveforms shown in (c). The velocity waveforms computed from strain are comparable in amplitude and shape to those of the velocimeter station.

where indices 1 and 2 stand for the horizontal components, index 3 stands for the vertical component, and ω is the angular frequency. Under a diffuse field assumption, Perton et al. (2009) showed that the spectral energy ($E_i(\mathbf{x}, \omega)$) can be computed from the average autocorrelation of the wavefield components and is proportional to the imaginary parts of the Green's function:

$$E_i(\mathbf{x}, \omega) = \left\langle v_i(\mathbf{x}, \omega) v_i^*(\mathbf{x}, \omega) \right\rangle \propto -\omega \text{Im} \left[\mathcal{G}_{ii}(\mathbf{x}, \mathbf{x}, \omega) \right], \tag{3}$$

where $v_i(\mathbf{x}, \omega)$ is the velocity field in direction i at a point $\mathbf{x}$, the $*$ denotes the complex conjugate operator, and the brackets $\langle \cdot \rangle$ denote averaging over time. In the frequency domain, the product $v_i(\mathbf{x}, \omega) v_i^*(\mathbf{x}, \omega)$ equals the autocorrelation in the time domain. In the last term of equation (3), Im[·] indicates the imaginary part and $\mathcal{G}_{ii}(\mathbf{x}, \mathbf{x}, \omega)$ is the displacement Green's function due to the application of a unit point force in the direction i at a location $\mathbf{x}$. This equation (equation (3)) is the same used for classic ambient seismic field correlations (Shapiro & Campillo, 2004), but for the special case where the source and receiver are co-located.

Within this framework, Sánchez-Sesma et al. (2011) proposed a theoretical description of the H/V spectral ratio and suggested that it could be directly computed in terms of the ratio of the imaginary part of the Green's functions as

$$\frac{H}{V}(\mathbf{x}, \omega) = \sqrt{\frac{\text{Im} \left[\mathcal{G}_{11}(\mathbf{x}, \mathbf{x}, \omega) + \mathcal{G}_{22}(\mathbf{x}, \mathbf{x}, \omega) \right]}{\text{Im} \left[\mathcal{G}_{33}(\mathbf{x}, \mathbf{x}, \omega) \right]}}. \tag{4}$$

DAS measurements only describe the component of motion along the fiber, which prevents the use of equation (2); however, under the diffuse field assumption, and in the absence of strong horizontal heterogeneity or lateral anisotropy (i.e., fault zone or basin edge), the horizontal spectral energies should be equal

regardless of their orientation (Perton et al., 2009). Therefore, equation (4) can be simplified as

$$\frac{H}{V}(\mathbf{x}, \omega) = \sqrt{\frac{2\text{Im}(\mathcal{G}_{11}(\mathbf{x}, \mathbf{x}, \omega))}{\text{Im}(\mathcal{G}_{33}(\mathbf{x}, \mathbf{x}, \omega))}}, \tag{5}$$

where the horizontal DAS measurement is used for the numerator. Because the vertical component of motion is expected to be relatively insensitive to the local site conditions (e.g., Campillo et al., 1989; Langston, 1979; Sánchez-Sesma et al., 1993; Yu et al., 2019), especially for a spatially limited region, the vertical component of a nearby velocimeter can be used as the denominator in equation (5). If both DAS ($v_{hori.}^{DAS}$) and velocimeter ($v_{vert.}^{vel.}$) recordings share same units (i.e., after conversion to velocity) the HVSR with DAS can be computed as

$$\frac{H}{V}(\mathbf{x}, \omega) = \sqrt{\frac{2\langle\left|v_{hori.}^{DAS}(\mathbf{x}, \omega)\right|^2\rangle}{\langle\left|v_{vert.}^{vel.}(\mathbf{x}, \omega)\right|^2\rangle}}. \tag{6}$$

Computing the H/V spectral ratio with DAS (equation 6) relies on two major assumptions: (i) that a single horizontal component yields a reliable spectral ratio and (ii) that we can use only one vertical component for a spatially extended distribution of horizontal components. The reliability of these assumptions is analyzed in the next sections through a series of examples in which we compare the Green's functions and the ratios computed using (1) the three components of a velocimeter located on campus and (2) a combination of horizontal DAS and vertical velocimeter components (equation (6)).

2.3.2. Computing the Green's functions

Equations (3) to (6) are only valid when the seismic wavefield is equipartitioned, that is, all the incident waves have the same energies (Perton et al., 2016). As this assumption is unlikely to be true, the equipartitioning of the seismic wavefield must be enhanced through signal processing, just as for traditional ambient seismic field cross correlation (e.g., Bensen et al., 2007; Spica et al., 2016).

As in Spica et al. (2018), we first remove the contribution of nonstationary sources such as transients and small earthquakes by applying a running absolute mean normalization in the time domain. We then apply spectral whitening, which corresponds to source deconvolution (Perton et al., 2017). Because several sources can act in different frequency bands and with different energy for the horizontal or the vertical component (Figure 2), the operation consists of normalizing the signals by the source energies computed in each time window and across several frequency bands. It is computed as

$$\tilde{v}_i(\mathbf{x}, \omega) = v_i(\mathbf{x}, \omega)/\sqrt{\int_{\omega-\Delta\omega/2}^{\omega+\Delta\omega/2} 2|v_{hori.}^{DAS}(\mathbf{x}, \omega)|^2 + |v_{vert.}^{velo.}(\mathbf{x}, \omega)|^2 d\omega}, \tag{7}$$

where $\Delta\omega$ is a frequency band of 0.7 Hz width centered on ω. Here, the particle velocity is taken in each time window as $v_x(\omega) = -c_{R_0}(\omega)\varepsilon_{xx}(\omega)$ with $c_{R_0}(\omega)$ being the reference dispersion curve for central campus. To remove only the spectral envelope, the bandwidth has to be much larger than the oscillations in the spectra (Figure 4; Perton et al., 2009, 2017, 2019) and because the DAS and velocimeter channels are not co-located, the time window should be large enough to allow the effect of sources to pass across the array. In this experiment the time window was set to 20 s with an overlap of 80%. Each window was then stacked over 1 day of data. Both the running absolute mean normalization and the whitening tend to equalize the spectral energies and enhance the equipartitioning. It is an essential component of the data processing that also tends to reduce the gap in sensitivity between DAS and velocimeter measurements. In that sense, the processing we apply to the data is substantially different than other studies that compute H/V spectral ratio following Nakamura (1989).

Figure 4a shows the displacement Green's function for the three components of velocimeter AC07 and Figure 4b for the two orthogonal DAS channels (85 and 185) located at the crossing of the cable along Via Ortega (Figure 1). The two horizontal components of the velocimeter share similar characteristics between themselves and with the two orthogonal components of DAS, which supports assumption (i) and suggests the absence of strong lateral heterogeneity next to the site; however, the DAS measurements (Figure 4b) undergo fewer spectral oscillations after the main frequency peak around 1 Hz. Perton et al. (2009) and
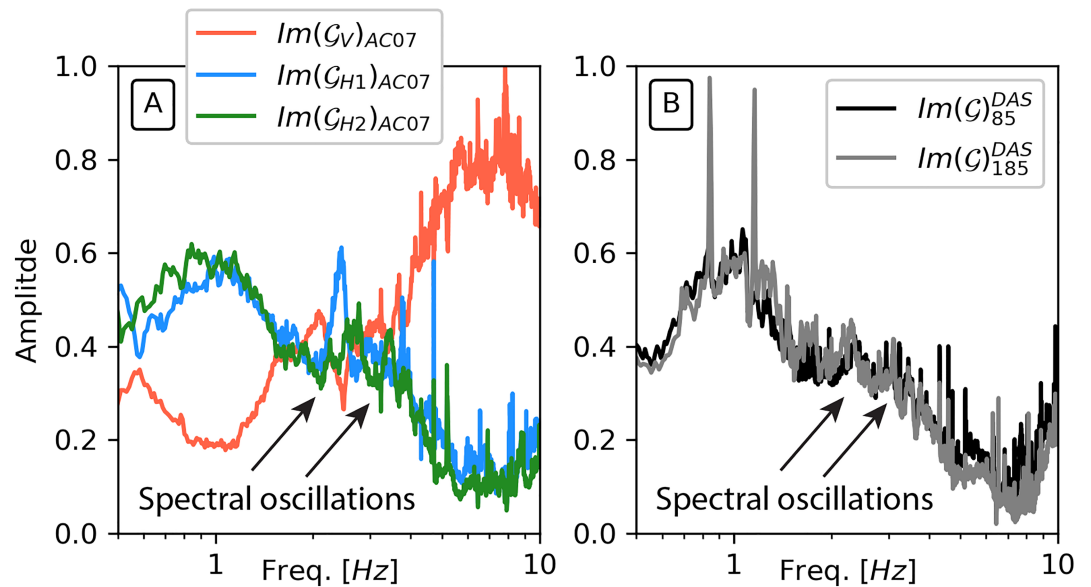
Figure 4. Single component Green's functions for DAS and velocimeter. (a) $Im(\mathcal{G}_{ii})$ computed from the tri-axial AC07 velocimeter and (b) computed for the two orthogonal channels 85 and 185.

Piña-Flores et al. (2016) showed that these small oscillations are likely related to the body wave contributions in the Green's function, while the main peak is related to the Rayleigh contribution. This is because the velocity-converted DAS Green's function contains a lower proportion of body waves than the Green's function computed with the velocimeter. We also observe that channel 185 presents a series of high amplitude spikes, which makes it less suitable for our analysis as it results in a distorted HVSR curve (Figure 5a). These spikes could be attributable to different coupling of the cable at this channel or to transient recording problems.

2.3.3. The Ratio of Green's Functions

We compute the H/V spectral ratios in terms of the wavefield auto correlations following equation (4) for the tri-axial velocimeter and using equation (6) for the DAS-velocimeter combination. In what follows, we refer to V-HVSR for the ratios computed with a tri-axial velocimeter and to D-HVSR for the ratios computed by combining DAS and velocimeter measurements.

Figure 5a compares three different spectral ratios: (1) V-HVSR at station AC07; (2) D-HVSR computed with channel 185 over the vertical component of station AC07; and (3) D-HVSR computed with channel 85 over the vertical component of station AC07. We observe that the overall shape and amplitude of the spectral ratios are very similar. Because the horizontal displacement Green's functions (Figure 4b) look alike and the vertical displacement Green's function used for deconvolution is the same (Figure 4a), removing the spikes in channel 185 (e.g., with a notch filter) should lead to a very similar D-HVSR curve. The D-HVSR curves peak at slightly higher frequency (∼1.2 Hz) than the V-HVSR (∼1.0 Hz). Such a difference is reasonable since along Via Ortega the D-HVSR frequency peaks vary by up to 0.33 Hz (Figure 5c). The V-HVSR presents a slightly broader peak than the D-HVSR. Because the velocimeter and DAS measurements are not co-located, it is difficult to conclude whether these subtle changes in shape are related to intrinsic properties of the underlying structure or whether it comes from the measurement. The good overall agreement of the measurements, however, supports our analysis and the assumptions behind it. The comparable level of instrumental noise over ∼0.3 Hz (Figure S1) further suggests the measurement is of similar quality. Note that the velocimeters are all located in the basements of buildings about 6 m below grade, but on top of thick building foundations, while DAS cable is laying typically 1 m below the surface in a PVC conduit. The thick foundation and the much better coupling of the velocimeter with the ground are likely to provide better low frequency retrieval of the horizontal components that might cause the small discrepancy between measurements, although it is also true that observations within buildings are susceptible to cultural noise.

In Figure 5b, we show three different D-HVSR for channel 85, computed with the vertical component of the three different velocimeters present on campus along with the V-HVSR for station AC07. We observe that
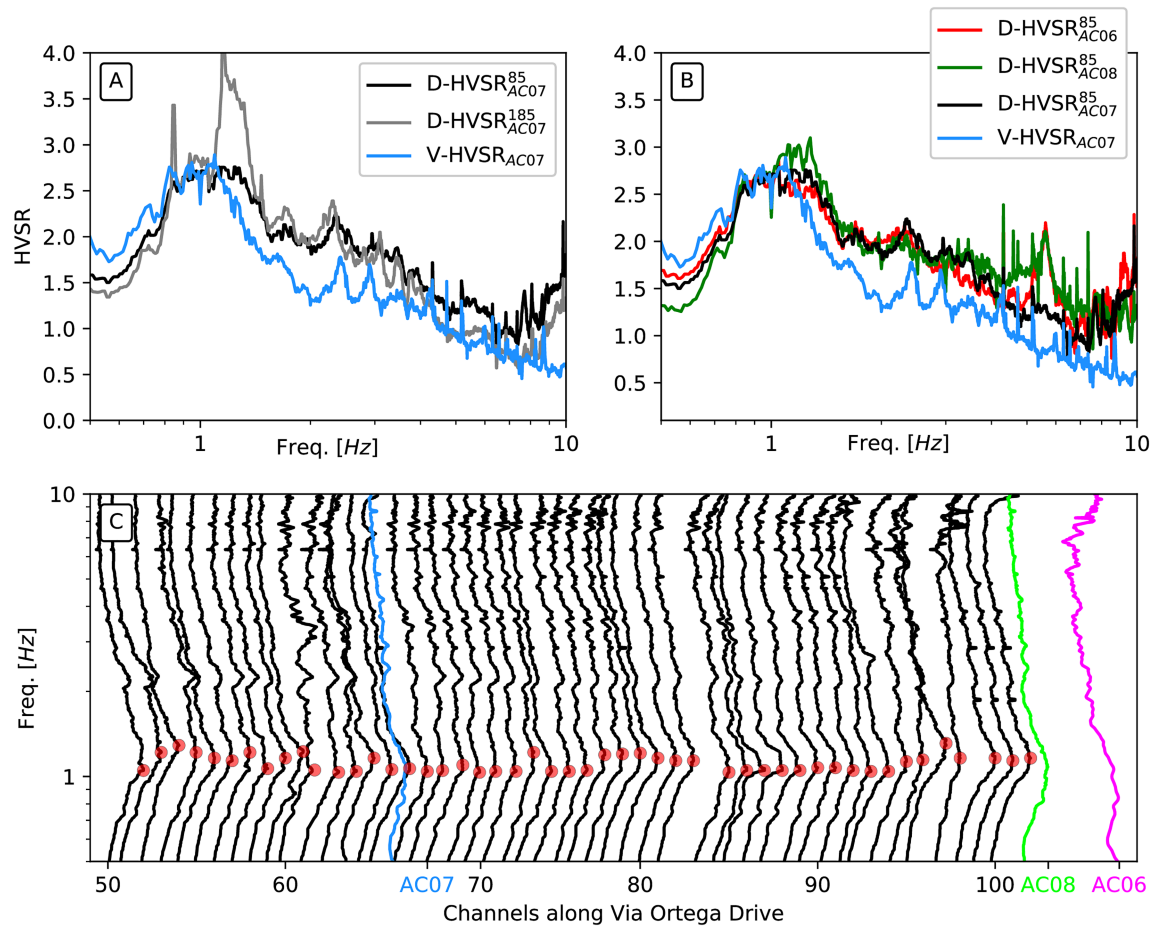
Figure 5. Comparison between DAS and velocimeter H/V spectral ratios. (a) D-HVSR computed with channels 85 and 185 and V-HVSR for station AC07. (b) Comparison between the V-HVSR at station AC07 and the D-HVSR at channel 85 computed with the vertical component of the three different velocimeters on campus. (c) All the D-HVSR computed along Via Ortega (black) along with the three V-HVSR (color). The frequency of the main D-HVSR peaks are highlighted by a red dot.

only the amplitude but not the shape of the D-HVSR curve is affected by the deconvolution of the vertical component. As expected for such a small scale experiment, the local site conditions are weakly sensitive to the vertical component motion such that it has only a minor effect on the shape of the D-HVSR. In the next analysis, we compute the D-HVSR using the vertical component of velocimeter AC07 because it is closest to the Via Ortega sub-array.

We observe small oscillations on both the D-HVSR and V-HVSR around 2.5 Hz in Figures 5a and 5b. These oscillations in D-HVSR suggest that the deconvolution with the vertical component of the velocimeter carries the signature of the body waves. While surface waves propagate in 2-D space and are generally not strongly scattered by lateral heterogeneity, body waves propagate in 3-D space and are reflected by the free surface and also by strong impedance contrasts at depth. As shown theoretically by Perton et al. (2009) for a half space, the waves traveling vertically up and down interfere and result in spectral oscillation periods in the energy density components (E_1, E_2, and E_3 in equation (2)). They showed that the amplitude of these oscillations in the H/V spectral ratio tends to decay with higher frequencies and that the $H = \sqrt{E_1 + E_2}$ is sensitive to the shear-wave velocity while $V = \sqrt{E_3}$ is mainly sensitive to the compressional wave velocity. We clearly observe such a pattern in our measurements, suggesting that the k/ω transformation from strain to particle velocity does not dramatically affect the final shape of the D-HVSR measurements. This is because an important proportion of body waves remains present in the vertical component of the velocimeter used for deconvolution of the horizontal DAS component.

Figure 5c shows all the D-HVSR computed at each channel along Via Ortega along with the V-HVSR for the three velocimeters (colored lines). As highlighted by Ajo-Franklin et al. (2019), the local conditions of
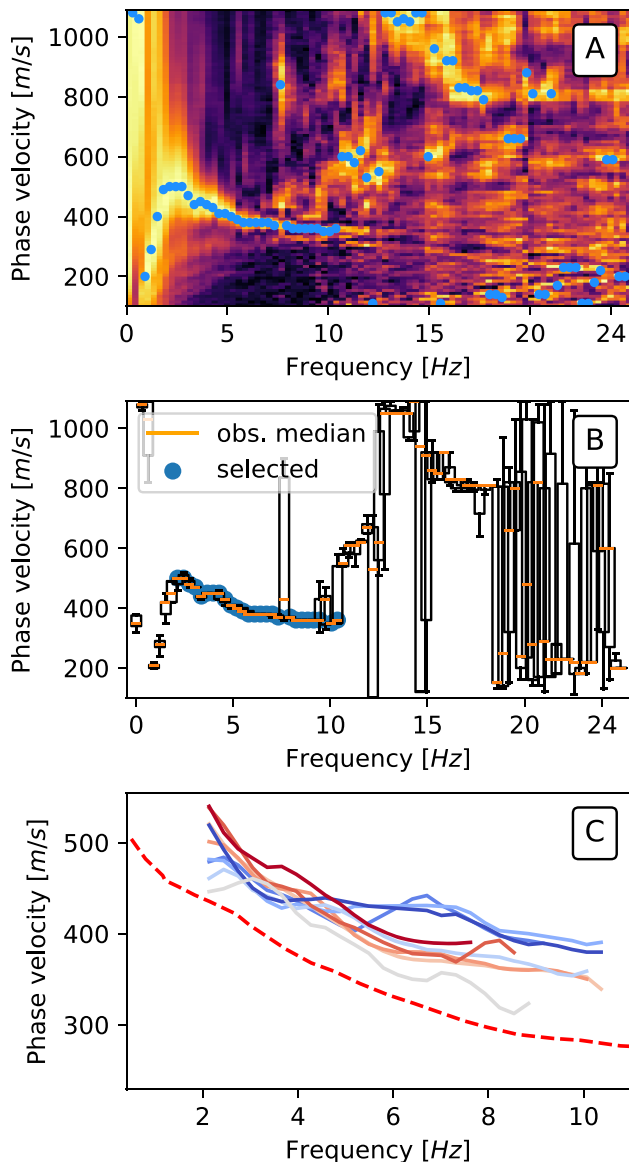
Figure 6. Dispersion curve analysis. (a) Rayleigh wave dispersion image for month-long cross correlations from the channels inline with virtual sources at channel 85. Yellow denotes more energy traveling at a particular frequency and velocity. Dark areas have less energy. The fundamental mode Rayleigh wave is particularly clear. Dots mark local peak velocities. (b) Distribution of each pick's variability versus frequency and velocity. The size of the vertical error bars reflects the variability of the measurement at each frequency. (c) Selected dispersion curves along Via Ortega. The color code refers to their position along Via Ortega. The warmer the color, the farther north along the array is the observed dispersion curve. For comparison, synthetic dispersion curve from a velocity model in central campus and shown in Figure S3 is also shown here in red dotted line.

the fiber can sometimes compromise continuous measurement along the fiber. Figure 5c shows that except for two channels (82 and 97), all sensors are able to recover the main frequency peak along Via Ortega with some variation. The main frequency peaks are highlighted by a red dot and vary from 1.12 to 1.45 Hz. It appears that the fundamental frequency of resonance varies smoothly over central campus suggesting a likely homogeneous geological structure (at this scale) under the DAS array. For stations AC07 and AC08, the main peak is at about 1 Hz while AC06 shows a flat V-HVSR curve, suggesting a lower velocity contrast at depth for this location and for the analyzed frequency range. The latter is further suggested by Figure S2, which shows a subset of D-HVSR along Via Pueblo. Next to channel 213, a clear change in the D-HVSR curve is observed and the main frequency peaks start to be less pronounced.

Overall, the good agreement between V-HVSR and D-HVSR validates the methodology and the processing and provides constraints on potential resonance frequencies at sites across campus.

2.4. Dispersion Curves

We apply passive Rayleigh wave interferometry to the DAS channels along Via Ortega using 1 year of continuous data starting from early September 2016 (Martin et al., 2017). Only a collinear sub-array is used for interferometry because that virtual-source configuration is expected to yield Rayleigh waves (Martin et al., 2018). We apply cross correlation of ambient seismic field with minimal preprocessing. We window of continuous signal into 5 min intervals with 50% overlap, band-passed filter from 0.5 to 24 Hz, perform a 1-bit normalization, and then stack hourly cross correlations. After saving each hour's average cross correlations throughout the week, we normalized them by their L1 norms and stack them for each month, yielding a series of virtual-source response estimates (Martin et al., 2017).

We calculate Rayleigh wave phase dispersion images from month-long virtual-source response estimates via tau-p transforms followed by a Fourier transform in tau. These dispersion images (Figure 6a) tell us how much energy is traveling at each velocity for a given frequency. For example, at 5 Hz the velocity at channel 85 is 440 m/s, and based on sensitivity analysis such a wave should be sensitive to features in the top ~70 m (Martin, 2018). These measurements are repeated for each month-long virtual-source response estimate, and based on their variability with time, we discard unstable frequencies from further analysis. This variability can be seen when plotting the distribution of picks from dispersion images of multiple virtual source gathers (Figure 6b). We observe very stable results from ~1.5 Hz up to 8–10 Hz, depending on the virtual source. Because of the limited aperture of the array, dispersion images are unreliable below 1.5–2 Hz.

We computed stable dispersion curves every five channels from channel 55 to 95. Only nine dispersion curves are computed in order to provide sufficient array size for dispersion analysis while still allowing for some degree of latera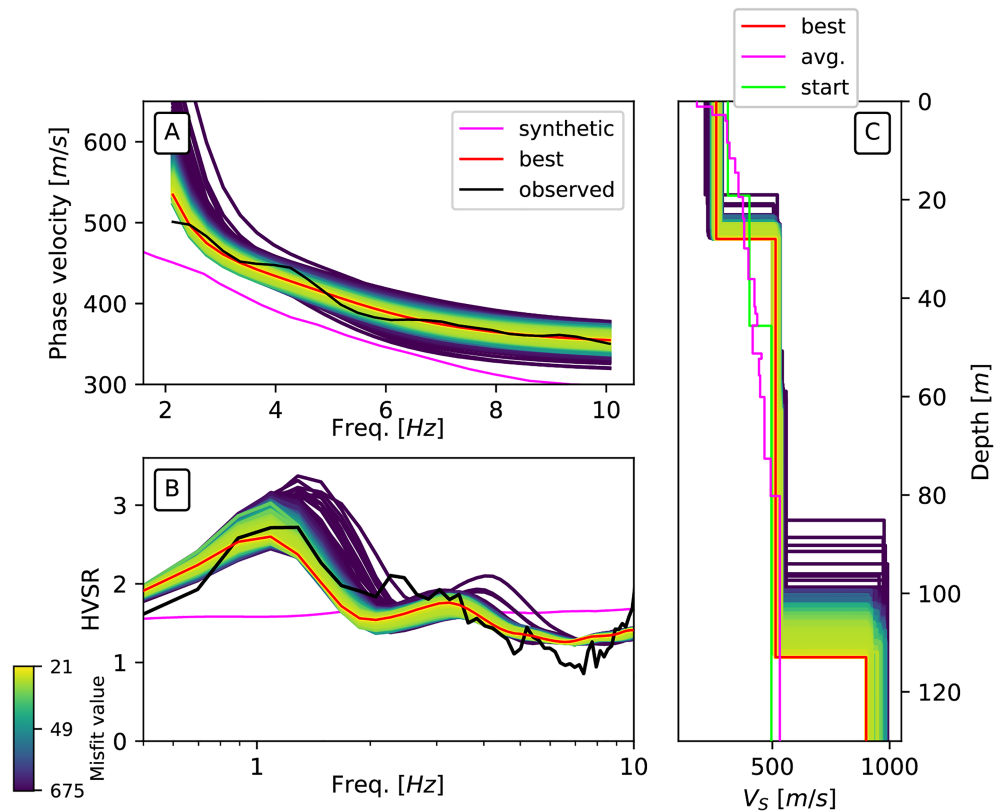l variation. Dispersion curves for other parts of the campus (i.e., Via Pueblo) were also computed; however, due to the strong directivity of the high-frequency ambient seismic field, they showed much larger variability in their velocity and were therefore not used for structure characterization (Martin & Biondi, 2018). Each extracted dispersion curve is shown in Figure 6c and compared with a synthetic dispersion curve from an independent averaged velocity model obtained by (Thomas et al., 2014) (Figure S3). The misfit between synthetic and observed velocities is about 50 to 100 m/s. This variation is reasonable given that throughout the Via Ortega fiber, dispersion curves vary by up to 100 m/s.

Figure 7. Joint inversion result for channel 85. (a) Dispersion curves. (b) D-HVSR. (c) V_S profiles. Starting velocity model is shown in lime green and is an harmonically averaged version of the model of Thomas et al. (2014) shown in pink. For comparison, synthetic dispersion curve and HVSR computed from the model of Thomas et al. (2014) are shown in pink in (a) and (b), respectively. Due to the absence of strong velocity contrast in this model, synthetic HVSR appear more flat.

Furthermore, in other parts of campus, V_s profiles in the top 100 m computed by Thomas et al. (2014) vary by up to 150 m/s from their local average.

2.5. Joint Inversion and Shallow V_S Estimates

In equation (4), the $\mathrm{Im}(\mathcal{G}_{ii})$ components are associated with the shallow local structure, which we approximate locally with a horizontally layered geometry having material properties (V_S) that vary only with depth; however, as the fundamental mode of the Rayleigh wave dominates the ambient seismic field (Figure 2), the direct problem used to compute the $\mathrm{Im}(\mathcal{G}_{ii})$ should account for it. Among the several methods that exist to compute these $\mathrm{Im}(\mathcal{G}_{ii})$ under a diffuse field assumption (e.g., Bouchon, 2003; García-Jerez et al., 2016; Perton et al., 2016, 2017), we use the analytical representation proposed by García-Jerez et al. (2016) because it allows us to compute the individual contribution of the various wave propagation modes. For example, we are able to compute the $\mathrm{Im}(\mathcal{G}_{ii})$ considering only the first higher mode Rayleigh wave (no Love waves) along with body waves, which allows us to better follow our assumptions.

It is well known that consideration of H/V solely at the surface is insufficient to characterize shallow properties uniquely due a trade-off between layer velocity and thickness that leads to a similar H/V curves (e.g., Scherbaum et al., 2003). Additionally, the forward problem is highly nonlinear and depends on several uncorrelated parameters (Lontsi et al., 2016; Hobiger et al., 2012). We therefore better constrain the inversion by inverting jointly the phase dispersion curve and the D-HVSR observations using a priori shear-wave velocities for central campus. The starting velocity model is a harmonically averaged version of the model of Thomas et al. (2014) (Figures 7 and S3). While the H/V spectral ratio is mainly sensitive to sharp impedance contrasts and vertical travel time, it has poor sensitivity to the absolute value of the velocities. On the other hand, dispersion curves are only weakly sensitive to the depth of structural variations due to the broad sensitivity kernels of surface waves with depth, but they are highly sensitive to the absolute velocity
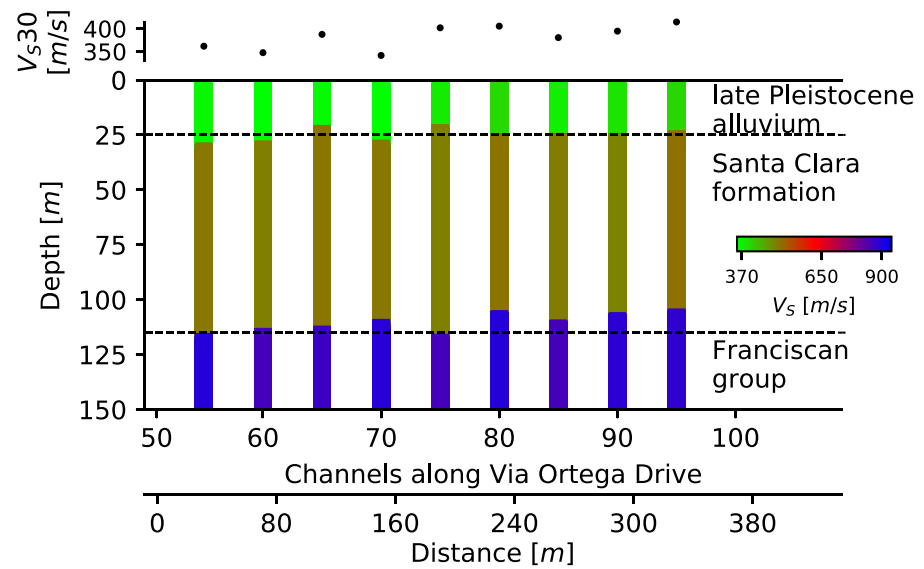
Figure 8. Joint inversion results and ground truth comparison. The black dashed lines correspond to lithological horizons as described in Thomas et al. (2014). The upper panel shows the V_S30 estimates extracted from the joint inversion results.

of the medium. The complementary nature of these measurements makes it a powerful combination for subsurface characterization (e.g., Perton et al., 2019; Picozzi et al., 2005).

In the inversion, both the shear-wave velocity and the layer thickness were the free parameters. A combination of Monte Carlo sampling and downhill simplex optimization was used to adjust the theoretical dispersion curve and D-HVSR. We found that only two layers over a half space were sufficient to fit the observed data. In the inversion, the weights between HVSR and DC are the same. More details of the inversion scheme can be found in Piña-Flores et al. (2016). An example of the inversion results is shown in Figure 7 for channel 85. Overall, the agreement for both D-HVSR and the dispersion curve is very good, although below 3 Hz the agreement of the dispersion curve is slightly worse, indicating some uncertainties with the velocity of the deeper structure. The averaged V_S model obtained from Thomas et al. (2014) is shown in magenta in Figure 7c. Although simpler, the shallow part of our velocity model agrees well with the velocity model. The main frequency peak around 1.2 Hz is well explained with a strong impedance contrast at about 115 m depth. Because the sensitivity of the dispersion curve at such depth is weak, but nonzero, the absolute velocity of the half space is not expected to be well constrained by our observations.

3. Discussion

3.1. Validation With Local Geology

Figure 8 shows all the velocity models computed along Via Ortega. The upper panel of Figure 8 also shows an estimate of the V_S30 for each site. These values are directly calculated from the joint inversion results. V_S30 is a widely used indicator of seismic site conditions and can be easily obtained from our joint inversion method.

While the values and the lateral variations of the V_S30 are useful information for geotechnical engineering, the depth of the basement is also important to characterize the site effect. To validate the reliability of our results, we compare them to local estimates made as part of an independent geotechnical study on campus (Thomas et al., 2014) and interpret them in terms of the local lithology.

The campus is covered by stiff late Pleistocene alluvial deposits (silty and sandy clay and dense gravelly silty sand) which vary in thickness from few meters at the southwest end of the campus to about 40 m at the northeast end (Thomas et al., 2014). Assuming it increases linearly between these extremes, the thickness of these deposits should be 20–25 m under central campus. Although it is a strong supposition, it is consistent with our observations.

These alluvia are underlain by the Santa Clara formation (very stiff to hard clays) to a depth of about 130 m (Knudsen et al., 2000; Witter et al., 2006). This formation is well represented by our velocity model although it has a slightly lower thickness. The absolute velocity of this formation (V_S ~500 m/s) matches well the results obtained by Thomas et al. (2014) for central campus (Figure 7c). In some places the Santa Clara formation is crosscut by the Merced Formation, which mainly consists of poorly consolidated sandstone and claystone. Our models suggests that this formation is either not present or has no clear seismic expression, under Via Ortega.

More controversy exists about the depth of the Franciscan group, which constitutes the local basement. Based on the bedrock contour map (Hazlewood, 1976) the Franciscan is expected to be ~330 m below the surface; however, the geotechnical survey suggested that it could lie at a much shallower depth (~30 to 90 m)—at least in the west campus area where a lithological layer with V_S velocity ranging from to 820 to 997 m/s was imaged (Thomas et al., 2014). Because of the survey design, only one velocity model (of 16) obtained from active source surveys reaches a depth of 100 m. Our velocity models display a strong velocity contrast at about 115 m depth. The velocities of the half space obtained from joint inversion of dispersion curve and D-HVSR agree with velocities of the Franciscan group observed on west campus by Thomas et al. (2014). Knowing the depth of the Franciscan group may significantly reduce uncertainty for site response analysis in central campus. These results suggest that our method allows us to obtain shallow velocity model with a reliability equal or superior to a traditional, dedicated geotechnical survey performed in an urban area.

3.2. Relevance to Ground Motion Prediction

For earthquake hazard analysis, engineers are required to estimate the shear-wave velocity in the upper 30 m of the subsurface. Knowledge of resonance frequencies is also important because they are the frequencies at which soft sediments are expected to amplify ground motion during a seismic event. Finally, the depth to bedrock/basement is also an important parameter for ground motion prediction simulations as seismic waves can be trapped by strong impedance contrasts. All this information in earthquake-threatened cities is generally sparse or nonexistent as it requires expensive and invasive seismic field campaigns. For this reason disaster risk assessment agencies often consider generic models of ground shaking intensity calibrated from observations of past earthquakes worldwide. Here, we demonstrate that existing fiber-optic cable network, otherwise used for communications, can also be used to transform the resolution of microzonation studies in highly populated areas and that it could do so in a cost-effective way.

Compared to previous studies that have discussed the potential of DAS for shallow subsurface characterization using dispersion curves, our results demonstrated the feasibility of computing H/V spectral ratio measurements from DAS recordings. H/V spectral ratio is an essential component of microzonation studies as it provides both the resonance frequency of a site and after inversion, a velocity model of the subsurface. In this contribution, we inverted dispersion curves and D-HVSR to resolve shallow shear velocities and the depth of the bedrock that conventional geotechnical survey failed to imaged.

By providing a local velocity model every 40 m, we offer a description of the shallow geotechnical layer and resonances at the scale of individual buildings. Increasing this lateral resolution appears to be possible and would open the pathway to analyze new models of ground motion variability. Considering a longer fiber cable offers the possibility of analyzing the variability of site-specific ground motion along distributed infrastructure related to energy, water, or transportation over long distances.

4. Conclusions and Future Implications

This study demonstrates the feasibility of H/V spectral ratio using a DAS-recorded ambient seismic field alongside a single velocimeter recording. We also show how to compute densely sampled Rayleigh wave dispersion curves (each 8 m) using DAS and illustrates the efficacy of such measurements for near-surface imaging in highly populated urban environments. Although results are acceptable for the specific case of the Stanford lithology, the many assumptions made on this research (e.g., single horizontal component, and same vertical component for the studied region) will have to be tested further and validated for more complex geological settings, which will likely require further developments. As a low-cost dense array, DAS could be a powerful system to assess site effects and the basement depth in other earthquake-threatened areas around the world, including mega-cities such as Mexico City, Tehran, Tokyo, or Djakarta that face extreme earthquake risk.

Data and Materials Availability

Due to the extremely large volume of data involved in this study (hundreds of Tb), only 1 day of DAS data for the station mentioned in this study has been uploaded on an open repository (Spica et al., 2019). These data will allow others to reproduce the measurements. The data from the broadband seismometers can be accessed at http://ds.iris.edu/gmap/#network=GM&planet=earth (last access June 2019). Code for joint inversion is accessible at https://w3.ual.es/GruposInv/hv-inv/ (last access June 2019).

References

Ajo-Franklin, J. B., Dou, S., Lindsey, N. J., Monga, I., Tracy, C., Robertson, M., et al. (2019). Distributed acoustic sensing using dark fiber for near-surface characterization and broadband seismic event detection. *Scientific Reports*, *9*(1), 1328.

Arai, H., & Tokimatsu, K. (2004). S-wave velocity profiling by inversion of microtremor H/V spectrum. *Bulletin of the Seismological Society of America*, *94*(1), 53–63.

Bard, P.-Y. (1998). Microtremor measurements: A tool for site effect estimation, *In Proceeding of the Second International Symposium on the Effects of Surface Geology on Seismic Motion* (Vol. 3, pp. 1251–1279). Rotterdam: AA Balkema.

Bensen, G. D., Ritzwoller, M. H., Barmin, M. P., Levshin, A. L., Lin, F., Moschetti, M. P., et al. (2007). Processing seismic ambient noise data to obtain reliable broad-band surface wave dispersion measurements. *Geophysical Journal International*, *169*(3), 1239–1260.

Beyreuther, M., Barsch, R., Krischer, L., Megies, T., Behr, Y., & Wassermann, J. (2010). ObsPy: A python toolbox for seismology. *Seismological Research Letters*, *81*(3), 530–533.

Biondi, B., Martin, E., Cole, S., Karrenbach, M., & Lindsey, N. (2017). Earthquakes analysis using data recorded by the Stanford DAS array. In *SEG Technical Program Expanded Abstracts* (pp. 2752–2756). https://doi.org/10.1190/segam2017-17745041.1

Bouchon, M. (2003). A review of the discrete wavenumber method. *Pure and Applied Geophysics*, *160*(3-4), 445–465.

Campillo, M., Gariel, J., Aki, K., & Sanchez-Sesma, F. (1989). Destructive strong ground motion in Mexico City: Source, path, and site effects during great 1985 Michoacán earthquake. *Bulletin of the Seismological Society of America*, *79*(6), 1718–1735.

Daley, T. M., Freifeld, B. M., Ajo-Franklin, J., Dou, S., Pevzner, R., Shulakova, V., et al. (2013). Field testing of fiber-optic distributed acoustic sensing (DAS) for subsurface seismic monitoring. *The Leading Edge*, *32*(6), 699–706.

Federal Emergency Management Agency (2003). NEHRP recommended provisions for seismic regulations for new buildings and other structures. Fema.

García-Jerez, A., Piña-Flores, J., Sánchez-Sesma, F. J., Luzón, F., & Perton, M. (2016). A computer code for forward calculation and inversion of the H/V spectral ratio under the diffuse field assumption. *Computers & Geosciences*, *97*, 67–78.

Grattan, K., & Sun, T. (2000). Fiber optic sensor technology: An overview. *Sensors and Actuators A: Physical*, *82*(1-3), 40–61.

Hazlewood, R. M. (1976). Contour map and interpretive cross sections showing depth and configuration of bedrock surface, south San Francisco Bay region, California (Technical Report): U.S. Geological Survey.

Heimann, S., Kriegerowski, M., Isken, M., Cesca, S., Daout, S., Grigoli, F., et al. (2017). *Pyrocko—An open-source seismology toolbox and library*. Potsdam: GFZ Data Services.

Hobiger, M., Cornou, C., Wathelet, M., Giulio, G. D., Knapmeyer-Endrun, B., Renalier, F., et al. (2012). Ground structure imaging by inversions of rayleigh wave ellipticity: Sensitivity analysis and application to european strong-motion sites. *Geophysical Journal International*, *192*(1), 207–229.

Hunter, J. D. (2007). Matplotlib: A 2D graphics environment. *Computing in Science and Engineering*, *9*(3), 90–95.

Jousset, P., Reinsch, T., Ryberg, T., Blanck, H., Clarke, A., Aghayev, R., et al. (2018). Dynamic strain determination using fibre-optic cables allows imaging of seismological and structural features. *Nature Communications*, *9*(1), 2509.

Knudsen, K. L., Sowers, J. M., Witter, R. C., Wentworth, C. M., & Helley, E. J. (2000). Description of mapping of quaternary deposits and liquefaction susceptibility, nine-county San Francisco Bay Region, California. Rep. No. United States Geologic Survey Open-File Report 00 444.

Langston, C. A. (1979). Structure under Mount Rainier, Washington, inferred from teleseismic body waves. *Journal of Geophysical Research*, *84*(B9), 4749–4762.

Lellouch, A., Horne, S., Meadows, M. A., Farris, S., Nemeth, T., & Biondi, B. (2019). DAS observations and modeling of perforation-induced guided waves in a shale reservoir. *The Leading Edge*, *38*(11), 858–864.

Lellouch, A., Yuan, S., Ellsworth, W. L., & Biondi, B. (2019). Velocity-based earthquake detection using downhole distributed acoustic sensing—Examples from the san andreas fault observatory at depthvelocity-based earthquake detection using downhole distributed acoustic sensing. Bulletin of the Seismological Society of America.

Lellouch, A., Yuan, S., Spica, Z., Biondi, B., & Ellsworth, W. (2019a). A moveout-based method for the detection of weak seismic events using downhole DAS arrays. In 81st EAGE Conference and Exhibition 2019.

Lellouch, A., Yuan, S., Spica, Z., Biondi, B., & Ellsworth, W. (2019b). Seismic velocity estimation using passive downhole distributed acoustic sensing records—Examples from the San Andreas fault observatory at depth, *124*, 6931–6948. https:doi.org/10.1029/2019JB017533

Lindsey, N. J., Martin, E. R., Dreger, D. S., Freifeld, B., Cole, S., James, S. R., et al. (2017). Fiber-optic network observations of earthquake wavefields. *Geophysical Research Letters*, *44*, 11,792–11,799. https:doi.org/10.1002/2017GL075242

Lontsi, A. M., Ohrnberger, M., Krüger, F., & Sánchez-Sesma, F. J. (2016). Combining surface-wave phase-velocity dispersion curves and full microtremor horizontal-to-vertical spectral ratio for subsurface sedimentary site characterization. *Interpretation*, *4*(4), SQ41–SQ49.

Lontsi, A. M., Sánchez-Sesma, F. J., Molina-Villegas, J. C., Ohrnberger, M., & Krüger, F. (2015). Full microtremor H/V (z, f) inversion for shallow subsurface characterization. *Geophysical Journal International*, *202*(1), 298–312.

Martin, E. R. (2018). Passive imaging and characterization of the subsurface with distributed acoustic sensing (open access PhD dissertation).

Martin, E. R., & Biondo, B. L. (2018). Eighteen months of continuous near-surface monitoring with DAS data collected under Stanford University. In *SEG Technical Program Expanded Abstracts* (pp. 4958–4962). https://doi.org/10.1190/segam2018-2997853.1

Martin, E., Biondi, B., Karrenbach, M., & Cole, S. (2017). Continuous subsurface monitoring by passive seismic with distributed acoustic sensors-the "Stanford array" experiment. In *15th International Congress of the Brazilian Geophysical Society & EXPOGEF, Rio de Janeiro, Brazil, 31 July-3 August 2017* (pp. 1366–1370). Brazilian Geophysical Society.

Martin, E. R., Castillo, C. M., Cole, S., Sawasdee, P. S., Yuan, S., Clapp, R., et al. (2017). Seismic monitoring leveraging existing telecom infrastructure at the SDASA: Active, passive, and ambient-noise analysis. *The Leading Edge*, *36*(12), 1025–1031.

Martin, E. R., Lindsey, N., Ajo-Franklin, J., & Biondi, B. (2018). Introduction to interferometry of fiber optic strain measurements. EarthArXiv.

Mateeva, A., Mestayer, J., Cox, B., Kiyashchenko, D., Wills, P., Lopez, J., et al. (2012). Advances in distributed acoustic sensing (DAS) for VSP. In *SEG Technical Program Expanded Abstracts* (pp. 1–5). https://doi.org/10.1190/segam2012-0739.1

Nakamura, Y. (1989). A method for dynamic characteristics estimation of subsurface using microtremor on the ground surface (in Japanese with english abstract). *Railway Technical Research Institute, Quarterly Reports*, *30*(1), 25–33.

Perton, M., Contreras-Zazueta, M. A., & Sánchez-Sesma, F. J. (2016). Indirect boundary element method to simulate elastic wave propagation in piecewise irregular and flat regions. *Geophysical Journal International*, *205*(3), 1832–1842.

Perton, M., Sánchez-Sesma, F. J., Rodríguez-Castellanos, A., Campillo, M., & Weaver, R. L. (2009). Two perspectives on equipartition in diffuse elastic fields in three dimensions. *The Journal of the Acoustical Society of America*, *126*(3), 1125–1130.

Perton, M., Spica, Z., & Caudron, C. (2017). Inversion of the horizontal-to-vertical spectral ratio in presence of strong lateral heterogeneity. *Geophysical Journal International*, *212*(2), 930–941. https://doi.org/10.1093/gji/ggx458

Perton, M., Spica, Z. J., Clayton, R. W., & Beroza, G. C. (2019). Shear wave structure of a transect of the los Angeles basin from multimode surface waves and H/V spectral ratio analysis. *Geophysical Journal International*, 220(1), 415–427. https://doi.org/10.1093/gji/ggz458

Piña-Flores, J., Perton, M., García-Jerez, A., Carmona, E., Luzón, F., Molina-Villegas, J. C., & Sánchez-Sesma, F. J. (2016). The inversion of spectral ratio H/V in a layered system using the diffuse field assumption (DFA). *Geophysical Journal International*, *208*, 577–588.

Picozzi, M., Parolai, S., & Richwalski, S. (2005). Joint inversion of H/V ratios and dispersion curves from seismic noise: Estimating the S-wave velocity of bedrock. *Geophysical Research Letters*, *32*, L11308. https:doi.org/10.1029/2005GL022878

Rivet, D., Campillo, M., Sanchez-Sesma, F., Shapiro, N. M., & Singh, S. K. (2015). Identification of surface wave higher modes using a methodology based on seismic noise and coda waves. *Geophysical Journal International*, *203*(2), 856–868.

Salinas, V., Luzón, F., García-Jerez, A., Sánchez-Sesma, F., Kawase, H., Matsushima, S., et al. (2014). Using diffuse field theory to interpret the H/V spectral ratio from earthquake records in Cibeles seismic station, Mexico City. *Bulletin of the Seismological Society of America*, *104*(2), 995–1001.

Sánchez-Sesma, F., Pérez-Rocha, L., & Reinoso, E. (1993). Ground motion in mexico city during the april 25, 1989, Guerrero earthquake. *Tectonophysics*, *218*(1-3), 127–140.

Sánchez-Sesma, F. J., Rodríguez, M., Iturrarán-Viveros, U., Luzón, F., Campillo, M., Margerin, L., et al. (2011). A theory for microtremor H/V spectral ratio: Application for a layered medium. *Geophysical Journal International*, *186*(1), 221–225.

Scherbaum, F., Hinzen, K.-G., & Ohrnberger, M. (2003). Determination of shallow shear wave velocity profiles in the Cologne, Germany area using ambient vibrations. *Geophysical Journal International*, *152*(3), 597–612.

Shapiro, N. M., & Campillo, M. (2004). Emergence of broadband Rayleigh waves from correlations of the ambient seismic noise. *Geophysical Research Letters*, *31*, L07614. https:doi.org/10.1029/2004GL019491

Sladen, A., Rivet, D., Ampuero, J.-P., Hello, Y., Calbris, G., & Lamare, P. (2019). Distributed sensing of earthquakes and ocean-solid earth interactions on seafloor telecom cables. *Nature Communications*, *10*, 5777. https://doi.org/10.1038/s41467-019-13793-z

Spica, Z., Caudron, C., Perton, M., Lecocq, T., Camelbeeck, T., Legrand, D., et al. (2015). Velocity models and site effects at Kawah Ijen volcano and Ijen caldera (Indonesia) determined from ambient noise cross-correlations and directional energy density spectral ratios. *Journal of Volcanology and Geothermal Research*, *302*, 173–189. https://doi.org/10.1016/j.jvolgeores.2015.06.016

Spica, Z., Perton, M., Calò, M., Legrand, D., Córdoba-Montiel, F., & Iglesias, A. (2016). 3-D shear wave velocity model of Mexico and south US: bridging seismic networks with ambient noise cross-correlations (C^1) and correlation of coda of correlations (C^3). *Geophysical Journal International*, *206*(3), 1795–1813. https://doi.org/10.1093/gji/ggw240

Spica, Z. J., Perton, M., Martin, E. R., Beroza, G. C., & Biondi, B. (2019). Dataset used in "urban seismic site characterization by fiber-optic seismology" by Spica et al. in Journal of Geophysical Research: Solid Earth. http://doi.org/10.5281/zenodo.3549085

Spica, Z. J., Perton, M., Nakata, N., Liu, X., & Beroza, G. C. (2017). Site characterization at Groningen gas field area through joint surface-borehole H/V analysis. *Geophysical Journal International*, *212*(1), 412–421. https://doi.org/10.1093/gji/ggx426

Spica, Z., Perton, M., Nakata, N., Liu, X., & Beroza, G. C. (2018). Shallow V_s imaging of the Groningen area from joint inversion of multimode surface waves and H/V spectral ratios. *Seismological Research Letters*, *89*(5), 1720–1729. https://doi.org/10.1785/0220180060

Stanko, D., Markušić, S., Strelec, S., & Gazdek, M. (2017). HVSR analysis of seismic site effects and soil-structure resonance in Varaždin city (North Croatia). *Soil Dynamics and Earthquake Engineering*, *92*, 666–677.

Thomas, A. M., Spica, Z., Bodmer, M., Schulz, W. H., & Roering, J. J. (2019). Using a dense seismic array to determine structure and site effects of the two towers earthflow in northern California. *Seismological Research Letters*. https://doi.org/10.1785/0220190206

Thomas, P., Wong, I., Zachariasen, J., Darragh, R., & Silva, W. (2014). 2013 Update to the sites-pecific seismic hazard analyses and development of seismic design ground motions (Tech. Rep.). California: Stanford University.

Tumurbaatar, Z., Miura, H., & Tsamba, T. (2019). Site effect assessment in Ulaanbaatar, Mongolia through inversion analysis of microtremor H/V spectral ratios. *Geosciences*, *9*(5), 228.

USGS (2016). U.S. Geological Survey Networks. International Federation of Digital Seismograph Networks: Dataset/Seismic Network. https:doi.org/10.7914/sn/gm

Wang, H. F., Zeng, X., Miller, D. E., Fratta, D., Feigl, K. L., Thurber, C. H., & Mellors, R. J. (2018). Ground motion response to an ml 4.3 earthquake using co-located distributed acoustic sensing and seismometer arrays. *Geophysical Journal International*, *213*(3), 2020–2036.

Webster, P., Wall, J., Perkins, C., & Molenaar, M. (2013). Micro-seismic detection using distributed acoustic sensing. In *SEG Technical Program Expanded Abstracts 2013* (pp. 2459–2463) . https://doi.org/10.1190/segam2013-0182.1

Witter, R. C., Knudsen, K. L., Sowers, J. M., Wentworth, C. M., Koehler, R. D., Randolph, C. E., et al. (2006). Maps of quaternary deposits and liquefaction susceptibility in the central San Francisco Bay Region, California (Technical Report): U. S. Geological Survey.

Yu, C., Zhan, Z., Lindsey, N. J., Ajo-Franklin, J. B., & Robertson, M. (2019). The potential of DAS in teleseismic studies: Insights from the goldstone experiment. *Geophysical Research Letters*, *46*, 1320–1328. https://doi.org/10.1029/2018GL081195

Zeng, X., Lancelle, C., Thurber, C., Fratta, D., Wang, H., Lord, N., et al. (2017). Properties of noise cross-correlation functions obtained from a distributed acoustic sensing array at Garner Valley, California. *Bulletin of the Seismological Society of America*, *107*(2), 603–610.